Author/s:
Sulejman, SB;Wesemann, L;McCormack, M;Meng, J;Hutchison, JA;Priscilla, N;McColl, G;Read, K;Sim, W;Sukhorukov, AA;Crozier, KB;Roberts, A

Title:
Metasurfaces for Infrared Multimodal Microscopy: Phase Contrast and Bright Field

Date:
2025-03-19

Citation:
Sulejman, S. B., Wesemann, L., McCormack, M., Meng, J., Hutchison, J. A., Priscilla, N., McColl, G., Read, K., Sim, W., Sukhorukov, A. A., Crozier, K. B. & Roberts, A. (2025). Metasurfaces for Infrared Multimodal Microscopy: Phase Contrast and Bright Field. ACS Photonics, 12 (3), pp.1494-1506. https://doi.org/10.1021/acsphotonics.4c02097.

Persistent Link:
https://hdl.handle.net/11343/355880

Metasurfaces for infrared multi-modal microscopy: phase contrast and bright field - supporting information

Shaban B. Sulejman,[*,†] Lukas Wesemann,[†] Mikkaela McCormack,[‡] Jiajun Meng,[†] James A. Hutchison,[¶] Niken Priscilla,[†] Gawain McColl,[§] Katrina Read,[‖] Wilson Sim,[⊥] Andrey A. Sukhorukov,[#] Kenneth B. Crozier,[†,@] and Ann Roberts[*,†]

†*ARC Centre of Excellence for Transformative Meta-Optical Systems, School of Physics, The University of Melbourne, Victoria 3010, Australia*

‡*Dorevitch Pathology, Heidelberg, Victoria 3084, Australia*

¶*ARC Centre of Excellence in Exciton Science, School of Chemistry, The University of Melbourne, Victoria 3010, Australia*

§*Florey Institute of Neuroscience and The University of Melbourne, Parkville, VIC 3010, Australia*

‖*St Vincent's Private Hospital, East Melbourne, Victoria 3065, Australia*

⊥*School of Science, RMIT University, Melbourne, Victoria 3001, Australia*

#*ARC Centre of Excellence for Transformative Meta-Optical Systems (TMOS), Department of Electronic Materials Engineering, Research School of Physics, The Australian National University, Canberra, ACT 2601, Australia*

@*ARC Centre of Excellence for Transformative Meta-Optical Systems, Department of Electrical and Electronic Engineering, The University of Melbourne, Victoria, 3010, Australia*

E-mail: sulejmans@unimelb.edu.au; ann.roberts@unimelb.edu.au

Contents: 30 pages, 19 figures and 2 tables

Contents

S1 Theory

S1.1 Image processing

The fundamental concepts for the application of the metasurface to tunable multi-modal microscopy are briefly described in the main article. Here, the explanation is expanded to explain how the metasurface operates in the formation of images. Consider a source of monochromatic plane waves with an electric field $\vec{E}_s(x, y, z)$, wavelength λ and wave-vector $\vec{k}$ propagating along the z-axis. Assuming polarized light and ignoring vector effects for now for illustration, suppose that this source of light illuminates a semi-transparent sample located in the $z = 0$ plane with a transmission function $O(x, y) = O_0(x, y)e^{i\varphi(x,y)}$ in the Kirchhoff approximation. Here, $O_0(x, y)$ represents the amplitude features of the sample and $\varphi(x, y)$ represents the phase features. This defines an optical image in the $z = 0$ plane with an intensity profile given by $I_0(x, y) = |O(x, y)|^2 = |O_0(x, y)|^2$, which represents the bright field image of the sample. Visualizing the transparent features of the sample requires highlighting the phase shifts imparted onto the light transmitted through the sample, which can be modelled as,

$$\vec{E}_{\text{in}}(x, y) = O_0(x, y)e^{i\varphi(x,y)}\vec{E}_s(x, y) \ . \tag{S1}$$

The metasurface filters the spatial frequency components of an image in either the object plane of the sample, the image plane or any plane thereafter that differs only by a free-space phase shift from the object plane. The optical response of the metasurface in k-space is characterized by the optical transfer function, which is defined as the Fourier transform of its Green's function. In general, the optical transfer function is a rank-2 tensor (to

accommodate polarization) given in the $\{p, s\}$-polarization basis as,

$$H(k_x, k_y) = \begin{pmatrix} H_{pp}(k_x, k_y) & H_{ps}(k_x, k_y) \\ H_{sp}(k_x, k_y) & H_{ss}(k_x, k_y) \end{pmatrix} \ . \tag{S2}$$

The spatial frequencies k_x, k_y and $k_z = \sqrt{|\vec{k}|^2 - k_x^2 - k_y^2}$ are the Cartesian projections of $\vec{k}$, where $k_0 = |\vec{k}| = 2\pi/\lambda$ is the wavenumber. As in Ref.,[1] the spatial frequency components can be represented as a function of the spherical coordinates $(r = k_0, \theta, \phi)$,

$$\begin{aligned} k_x &= k_0 \sin(\theta) \cos(\phi) \\ k_y &= k_0 \sin(\theta) \sin(\phi) \\ k_z &= k_0 \cos(\theta) \ , \end{aligned} \tag{S3}$$

where (θ, ϕ) are the polar and azimuthal propagation angles of the plane waves with respect to the z-axis, respectively. Any light beam can be decomposed into bundles of weighted plane waves, each travelling in different directions, by the Fourier transform,[2]

$$\mathscr{F}\{E(x, y)\}(k_x, k_y) = \int_{-\infty}^{\infty} \int_{-\infty}^{\infty} E(x, y) e^{-i(k_x x + k_y y)} dx dy \ , \tag{S4}$$

where $\mathscr{F}$ is the Fourier transform operator. Also, given that the optical transfer function represents the response of the metasurface to plane waves in k-space, then it follows that the spatial frequency dependence of the metasurface in k-space is equivalent to an angular dependence in real space. This is the concept that is fundamental to the design of the metasurface.

The impact of the metasurface on an input image is determined by the Green's function of the metasurface. The output image is given by a convolution integral between the input

image and the Green's function,

$$E_i(x,y) = \int_{-\infty}^{\infty}\int_{-\infty}^{\infty} G_{ij}(x-x',y-y')E_j^{\text{in}}(x',y')dx'dy' \ , \tag{S5}$$

where $G(x,y)$ is the Green's function tensor and E_i is the i^{th}-component of the output electric field. However, by the convolution theorem, the impact of the metasurface on the spatial frequency spectrum of the input image can be directly modelled as,

$$\tilde{E}_i(k_x,k_y) = H_{ij}(k_x,k_y)\tilde{E}_j^{\text{in}}(k_x,k_y) \ , \tag{S6}$$

where $\tilde{E} = \mathscr{F}\{E\}$. The convolution theorem simplifies the relationship between the input image and the output image from a convolution in real space to a multiplication with the optical transfer function in k-space. The output electric field E can be recovered from $\tilde{E}$ by the inverse Fourier transform,

$$\mathscr{F}^{-1}\{\tilde{E}(k_x,k_y)\}(x,y) = \frac{1}{2\pi}\int_{-\infty}^{\infty}\int_{-\infty}^{\infty} \tilde{E}(k_x,k_y)e^{i(k_x x+k_y y)}dk_x dk_y \ , \tag{S7}$$

where $\mathscr{F}^{-1}$ is the inverse Fourier transform operator and $E = \mathscr{F}^{-1}\{\tilde{E}\}$. Therefore, given the following property for the Fourier transform of a derivative,

$$\mathscr{F}\left\{\frac{\partial E}{\partial x}\right\}(k_x,k_y) = ik_x\tilde{E}(k_x,k_y) \ , \tag{S8}$$

then a linear optical transfer function, $H \propto k_x$, can produce the spatial derivative (up to a multiplicative constant) of an incoming light field along the x-direction. It follows that a metasurface with an approximately linear angular dispersive transmission $T(\theta) \propto \sin(\theta) \approx \theta$ (for $\phi = 0$ and small values of θ) is capable of phase contrast imaging. Here, the $\{p, s\}$-polarization basis was used but, in general, the optical transfer function tensor can be expressed in any polarization basis. Henceforth, we utilize an $\{x, y\}$ basis, i.e. H_{xx}, H_{xy},

H_{yx} and H_{yy}, describing the impact of the metasurface on the transverse components of the incident field. It was shown in the main article that if we let the x-axis be aligned with the long axis of the silicon blocks for an un-tilted metasurface (normal incidence), then the metasurface has an approximately linear optical transfer function at a tilt of 2° about the y- (short) axis for x-polarized illumination, i.e. $H_{xx} \propto k_x + k_{x0}$, where k_{x0} is a constant. This can compute the derivative along the x-direction, plus a constant offset that pertains to a non-zero background in the output image. Hence, the design of the metasurface was carried out by optimizing the angular response of the metasurface in real space to engineer its optical transfer function in k-space.

In the case of a pure phase sample that has $|O_0(x, y)|$ = constant, then the sample is visualized because the phase derivative is converted into intensity variations in the output image $I(x, y)$,

$$I(x, y) \approx \left| O_0 \left(\frac{\partial \varphi(x, y)}{\partial x} + k_{x0} \right) \right|^2 . \tag{S9}$$

This result is obtained when a linear optical transfer function ($H_{xx} \propto k_x + k_{x0}$) and Eq. (S1) are substituted into Eq. (S6). Hence, the output image is proportional to $|\partial \varphi(x, y)/\partial x|^2$, with contrast created in regions where the phase is varying along the direction of differentiation. The constant offset in the optical transfer function is due to the metasurface being slightly tilted by 2°, corresponding to a normalized spatial frequency of $k_{x0}/k_0 \approx 0.03$, that shifts the k-space origin about the angular offset. The increased transmission level at this offset preserves some of the illumination to create a non-zero background in the output image. This distinguishes the imaging modality from dark field imaging that has a dark background in the output image. One could also uniquely distinguish the phase derivatives as they will manifest as different grayscale levels that are above or below the background, corresponding to the region of zero phase gradient, i.e. $I(x, y) \approx |O_0 k_{x0}|^2$.

On the other hand, the metasurface was approximately transparent when the illumination was y-polarized. This corresponds to a flat optical transfer function, $H_{yy} \approx$ constant, that only attenuates the input image. In the case that the constant is equal to one, the output

image will be exactly the input image. As a result, the output image is proportional to the bright field image, i.e. $I(x,y) \propto |O(x,y)|^2$. The cross-polarized components of the optical transfer function H_{xy} and H_{yx} (Fig. S7 and Table S1) are zero in the region of operation. However, they have some non-zero contributions for larger values of k_x and k_y, but these contributions were measured to be negligible in the experiments by using an analyzing polarizer on the output image.

The performance of the polarization switching was quantified by the switching contrast of the metasurface, defined as $\delta = H_{yy}(0,0) - H_{xx}(0,0)$. A similar value can be defined for the switching contrast of the transmittance, given by $\Delta = T_y - T_x$, where T_x and T_y are the transmittance levels under x- and y-polarized illumination at the operating wavelength, respectively. The efficiency of the metasurface for image processing is defined as $\eta = |H_{xx}(k_x^{\max}, 0)|$, where $k_x^{\max}$ is the maximum spatial frequency component where the optical transfer function of the metasurface is still within its numerical aperture. The numerical aperture of the metasurface, NA, is defined to be the width of the optical transfer function where the above conditions are met. This is contrasted from the numerical aperture of the imaging system itself, which is determined by the optical components in the system.

S1.2 Multipole decomposition

Fig. 2a-iii of the main article shows a multipole decomposition of the transmittance spectrum of the metasurface. The method from Ref.[3] was used to do this and it is briefly summarized here. Consider a metasurface composed of an array of identical dielectric resonators. For normally incident, x-polarized illumination, the multipole decomposition of the transmittance of the metasurface up to second order is given by,

$$T = \left| 1 + \frac{ik}{2E_0 A_{\text{cell}} \epsilon_0 \epsilon_s} \left(p_x + \frac{1}{v_s} m_y - \frac{ik}{6} Q_{xz} - \frac{ik}{2v_s} M_{yz} + \cdots \right) \right|^2 . \tag{S10}$$

Here, $k = 2\pi/\lambda$ is the wave-number in the surrounding, E_0 is the magnitude of the incident electric field, λ is the wavelength of the illumination, A_{cell} is the area of the lattice unit cell, ϵ_s is the relative permittivity of the surrounding and v_s is the speed of light in the surrounding. Furthermore, $\vec{p}$ is the electric dipole moment vector, $\vec{m}$ is the magnetic dipole moment vector, Q is the electric quadrupole moment tensor and M is the magnetic quadrupole moment tensor. The relevant components of the multipole moments are given by,

$$\begin{aligned} p_x &= \int P_x j_0(kr) dV + \frac{k^2}{10} \int \frac{15 j_2(kr)}{(kr)^2} \left((\vec{r} \cdot \vec{P}) x - \frac{1}{3} r^2 P_x \right) dV \\ m_y &= -\frac{i\omega}{2} \int \frac{3 j_1(kr)}{kr} \left(\vec{r} \times \vec{P} \right)_y dV \\ Q_{xz} &= \int \frac{9 j_1(kr)}{kr} \left(x P_z + P_x z \right) dV + 6k^2 \int \frac{j_3(kr)}{(kr)^3} \left(5xz(\vec{r} \cdot \vec{P}) - (x P_z + P_x z) r^2 \right) dV \\ M_{yz} &= \frac{\omega}{3i} \int \frac{15 j_2(kr)}{(kr)^2} \left((\vec{r} \times \vec{P})_y z + y (\vec{r} \times \vec{P})_z \right) dV \ , \end{aligned} \tag{S11}$$

where $\vec{r} = (x, y, z)$ is the position vector, j_n is the n^{th}-order spherical Bessel function of the first kind, $\vec{P}(\vec{r}) = \epsilon_0(\epsilon_s - 1)\vec{E}(\vec{r})$ is the polarization density and $\omega = 2\pi f$ is the angular frequency. The integrals are performed over the volume V of the resonator within a single unit cell of the metasurface. This formalism was set up in COMSOL Multiphysics 6.1 to obtain the multipole decomposition of the transmission spectrum of the metasurface.

S1.3 Mie scattering of an isolated resonator

In 1908, Gustav Mie[4] exactly solved Maxwell's equations for the scattering of plane waves from a homogeneous sphere of size comparable to a wavelength. Although the analytic solution exists only for ellipsoidal particles, the physics is identical for arbitrary geometries.[5] Consider the Mie scattering of plane waves by a rectangular resonator. To characterize its multipolar behaviour, the electric field scattered by the resonator when under plane wave

illumination is expanded in the basis of vector spherical harmonics,

$$\vec{E}_{sc}(r,\theta,\phi) = \sum_{n=1}^{\infty}\sum_{m=-n}^{+n} c_{nm}\left(a_{nm}\vec{N}_{nm}(r,\theta,\phi) + b_{nm}\vec{M}_{nm}(r,\theta,\phi)\right) \ , \tag{S12}$$

where a_{nm} and b_{nm} are the electric and magnetic scattering coefficients, respectively. The normalization constants are defined as,

$$c_{nm} = |\vec{E}_0| i^{n+2m-1}\sqrt{\frac{(2n+1)(n-m)!}{4(n+m)!}} \ , \tag{S13}$$

where $\vec{E}_0$ is the electric field of the illumination. Following the formalism from Ref.,[6] the electric and magnetic harmonics are respectively defined in spherical coordinates as,

$$\begin{aligned}\vec{N}_{nm} = \frac{1}{k_0 r}\Bigg(\tau_{nm}(\cos(\theta))\hat{\theta} + i\pi_{nm}(\cos(\theta))\hat{\phi}\Bigg)e^{im\phi}\frac{\partial}{\partial r}\Bigg(r h_n^{(1)}(k_0 r)\Bigg) \\ + \frac{n(n+1)}{k_0 r}P_n^m(\cos(\theta))h_n^{(1)}(k_0 r)e^{im\phi}\hat{r} \\ \vec{M}_{nm} = h_n^{(1)}(k_0 r)e^{im\phi}\Bigg(i\pi_{nm}(\cos(\theta))\hat{\theta} - \tau_{nm}(\cos(\theta))\hat{\phi}\Bigg) \ ,\end{aligned} \tag{S14}$$

where $h_n^{(1)}$ is the n^{th}-order spherical Hankel function of the first-kind and P_n^m is the n^{th}-order associated Legendre polynomial of degree m. The τ and π functions are defined as,

$$\begin{aligned}\tau_{nm}(\theta) &= \frac{\partial}{\partial\theta}P_n^m(\cos(\theta)) \\ \pi_{nm}(\theta) &= mP_n^m(\cos(\theta))\csc(\theta) \ .\end{aligned} \tag{S15}$$

The scattering coefficients can be computed by projecting the scattered electric field onto the vector spherical harmonics on a virtual sphere of radius r_0 surrounding the resonator, given by,

$$\begin{aligned}a_{nm} &= \frac{\int_0^{2\pi}\int_0^{\pi}\vec{E}_{sc}(r=r_0,\theta,\phi)\cdot\vec{N}^*_{nm}(r=r_0,\theta,\phi)\sin(\theta)d\theta d\phi}{c_{nm}\int_0^{2\pi}\int_0^{\pi}|\vec{N}_{nm}(r=r_0,\theta,\phi)|^2\sin(\theta)d\theta d\phi} \\ b_{nm} &= \frac{\int_0^{2\pi}\int_0^{\pi}\vec{E}_{sc}(r=r_0,\theta,\phi)\cdot\vec{M}^*_{nm}(r=r_0,\theta,\phi)\sin(\theta)d\theta d\phi}{c_{nm}\int_0^{2\pi}\int_0^{\pi}|\vec{M}_{nm}(r=r_0,\theta,\phi)|^2\sin(\theta)d\theta d\phi} \ .\end{aligned} \tag{S16}$$

By using the asymptotic relation $h_n^{(1)}(k_0 r) \sim (-i)^n e^{ik_0 r}/ik_0 r$ for $k_0 r \gg 1$ and the orthonormality of the associated Legendre polynomials, it follows that the scattering cross section is given by

$$\sigma_s = \frac{\pi}{k_0^2} \sum_{n=1}^{\infty} \sum_{m=-n}^{+n} n(n+1) \left(|a_{nm}|^2 + |b_{nm}|^2 \right) \ . \tag{S17}$$

The integer $n \in [1, \infty)$ provides the degree of the multipole, i.e. $n = 1$ corresponds to dipole, $n = 2$ to quadrupole, etc., while the integer $m \in [-n, n]$ provides their orientations in space. The contribution to the scattering cross section for each n represents the cross section for that particular degree of the multipole. Furthermore, for each multipole degree, the electric component corresponds to the a_{nm} term and the magnetic component to the b_{nm} term. Hence, the total cross section can be decomposed as,[7]

$$\sigma_s = \sigma_s^{ED} + \sigma_s^{MD} + \sigma_s^{EQ} + \cdots \ , \tag{S18}$$

where ED, MD and EQ each stand for electric dipole, magnetic dipole and electric quadrupole, respectively. The Mie resonances of the resonator manifest as peaks in the cross sections at the resonant wavelengths. This formalism was set up in COMSOL Multiphysics 6.1 to determine the multipolar decomposition of the scattering cross section for an isolated resonator from the metasurface.

S2 Additional simulation data

S2.1 Optical response

Simulations of the optical response of the metasurface were performed using the steps outlined in the Methods section of the main article. The metasurface was designed to have an angle-dependent transmission for x-polarized illumination at the operating wavelength, and an angle-independent transmission for y-polarized illumination. The angle-dependent transmission spectra are given in Fig. S1 as a function of the angle of incidence. The results

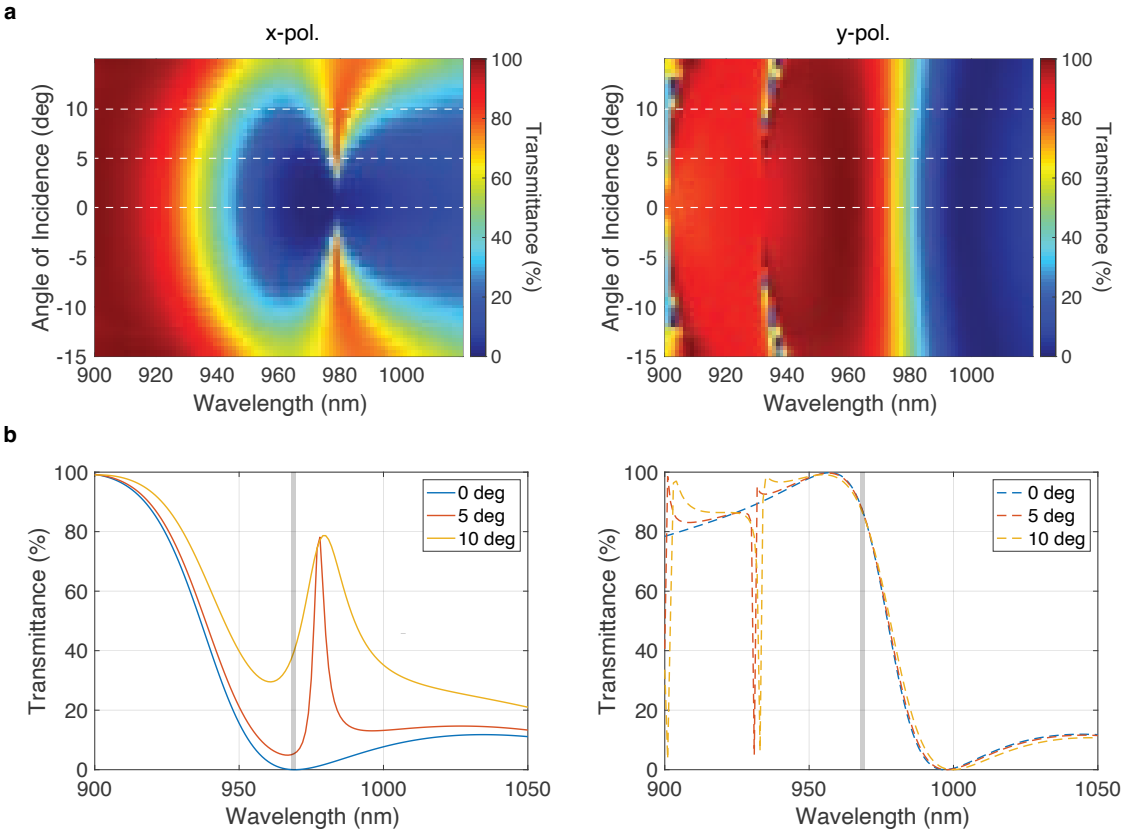

Figure S1: **Angle-dependent transmission spectra**. (a - left) A 2D heat map of the transmission versus the angle of incidence and the wavelength of x-polarized illumination. (a - right) Same as the left but for y-polarization. (b - left) The 1D transmission spectra for 0, 5 and 10 degrees angle of incidence for x-polarized illumination. (b - right) Same as the left but for y-polarized illumination.

show that the transmission spectrum changed under x-polarized illumination with a varying angle of incidence. Meanwhile, the transmission spectrum under y-polarized illumination remained similar when the angle of incidence was varied, with only the appearance of dark modes for shorter wavelengths.

The 1D plots of the optical response are given in Fig. S2. The reflectance of the metasurface is shown to be a maximum at the operating wavelength for x-polarized illumination and a minimum for y-polarized illumination (Fig. S2a). The absorptance is also shown to be nearly zero for both cases. The transmission spectra for different states of linear polarization shows how the spectrum morphs between those for x- and y-polarized illumination (Fig. S2b).

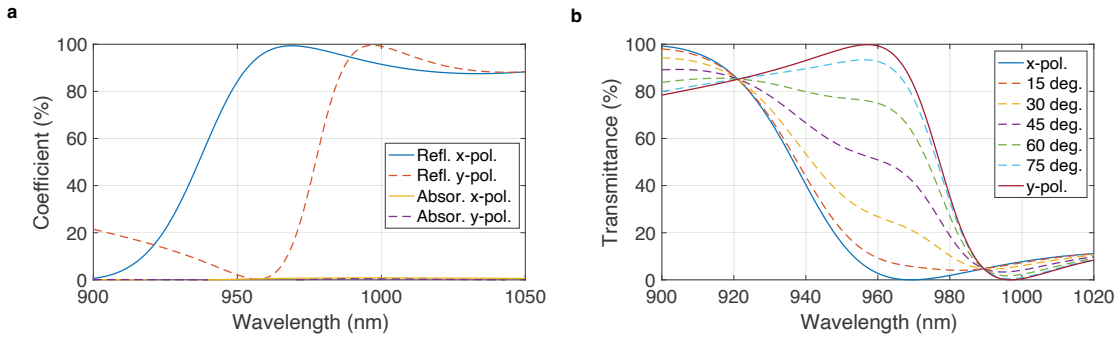

Figure S2: **1D spectra as a function of various parameters**. (a) The reflectance and absorptance spectra of the metasurface for x- and y-polarized illumination. (b) The transmittance spectra as a function of the angle of linear polarization.

The operating wavelength of the metasurface is dependent on the geometrical parameters of the metasurface, including the size of the resonators (length L, width W and height H) and the lattice constant (P) of the array. The dispersion of the resonance as a function of the geometrical parameters is shown in Fig. S3. In each case, the resonance red-shifted as the geometrical parameters were increased.

The electromagnetic behavior of the metasurface when on-resonance is depicted in Figs. S4-S6. They each show the electric field, magnetic field and power flow in the unit cell of the metasurface at the operating wavelength for x- and y-polarized illumination. The electric and magnetic fields when on-resonance from x-polarized illumination display behavior that is linked to an electric dipole resonance, with the power of the fields swirling around the resonator. On the other hand, the fields behave differently when off-resonance and the power of the fields flows through the resonator.

The magnitude and phase of the optical transfer function are given in Fig. S7. It was computed as the angle-dependent transmission as a function of the polar and azimuthal angles of incidence (θ, ϕ). The 1D slices through $k_x = 0$ and $k_y = 0$ are given in Fig. S8. The results show that the capability of the metasurface to process input images along k_y is weaker than that for k_x under x-polarization. Moreover, the cross-polarized components of the optical transfer function are consistent with Ref.[8] They are non-zero along the diagonals in Fig. S7(middle column), however the contribution to the output was measured to be small

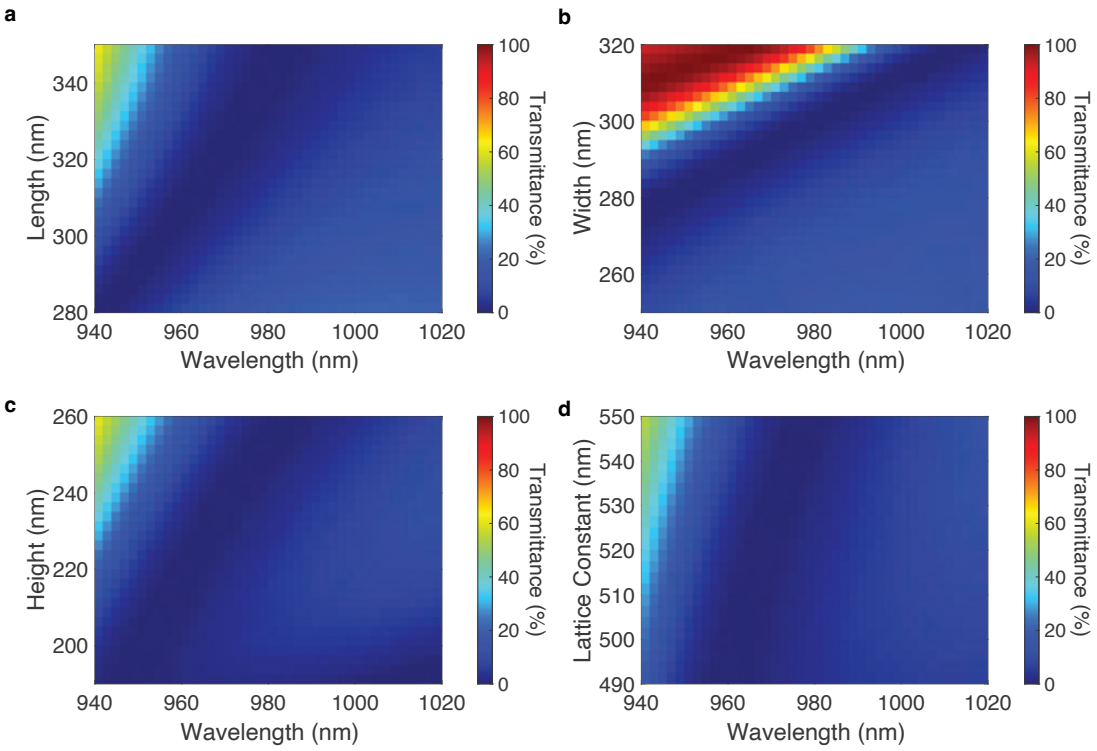

Figure S3: **Dispersion of the resonance**. (a) A 2D heat map of the transmittance spectrum as a function of the length of the resonators. (b) Same as a but for the width of the resonators. (c) Same as a but for the height of the resonators. (d) Same as a but for the lattice constant of the metasurface. In all cases, the illumination was x-polarized.

in the experiments.

S2.2 Performance metrics

The performance of the metasurface was quantified through various numerical metrics. These included the transmittance, reflectance, absorptance, quality factor, electric field enhancement, numerical aperture, angular response, polarization conversion efficiency, processing efficiency and the switching contrast. The results are tabulated in Table S1 and can be compared to the experimental results in Table S2. The results show that the metasurface strongly reflects light when on-resonance with little absorption for normally incident, x-polarized illumination. The electric dipole resonance had a quality factor of 17.3, which produced an optical transfer function with a numerical aperture of approximately 0.17.

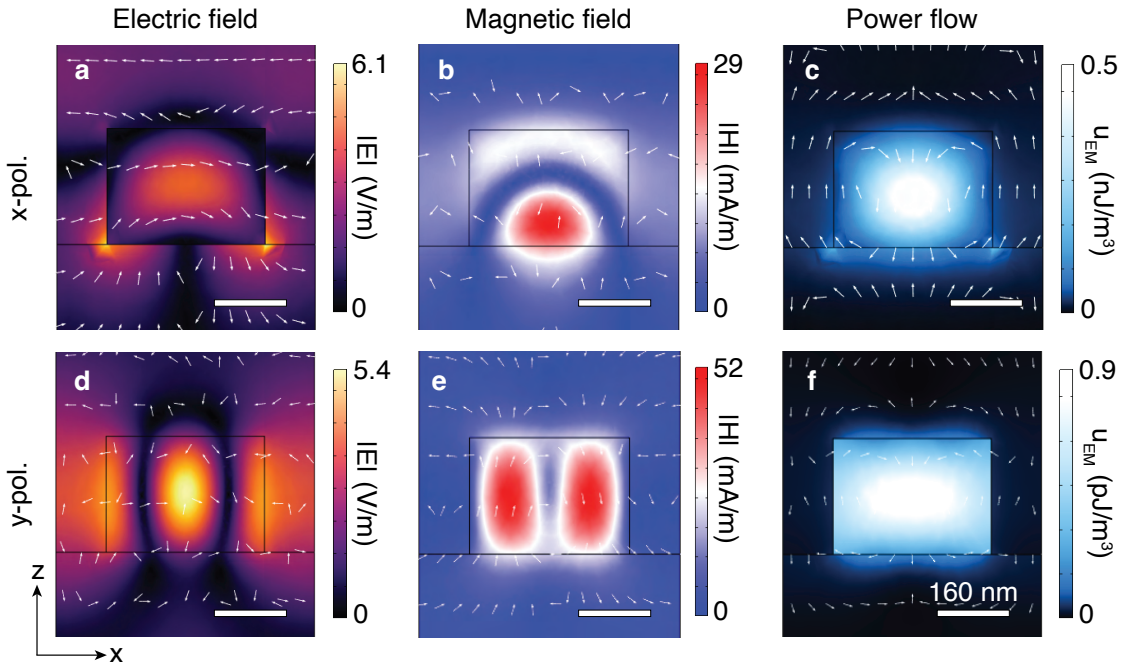

Figure S4: **Electromagnetic behavior of the metasurface in the xz-plane.** (a),(d) The electric field strength (heat map) and direction (arrows) in the unit cell for x- (a) and y-polarization (d). (b),(e) Same as (a),(d) but for the magnetic field. (c),(f) The time-averaged electromagnetic energy density (heat map) and Poynting vector (arrows) in the unit cell for x- (c) and y-polarization (f). All of the images are given in the xz-plane of the metasurface and at the operating wavelength.

S2.3 Isolated resonator

The optical response of an isolated silicon resonator of size given in the main article was investigated by implementing the formalism explained in section S1.2. The simulations were performed using the finite element method within the wave optics module of COMSOL Multiphysics 6.1. The scattering formulation was used to project the far-zone scattered electromagnetic field onto the vector spherical harmonics on a virtual sphere of radius $r_0 =$ 750 nm surrounding the resonator. Sommerfeld boundary conditions and a perfectly matched layer were applied onto the virtual sphere to remove unwanted reflections into the system and to simulate an open domain. The finite meshing elements in the model had a a minimum size of 5 nm and a maximum size of $\lambda/8$ nm. The perfectly matched layer had a series of 5 meshing elements. The scattering cross section was obtained by integrating the projections of the electromagnetic fields onto the vector spherical harmonics and using Eqs. (S10)-(S15).

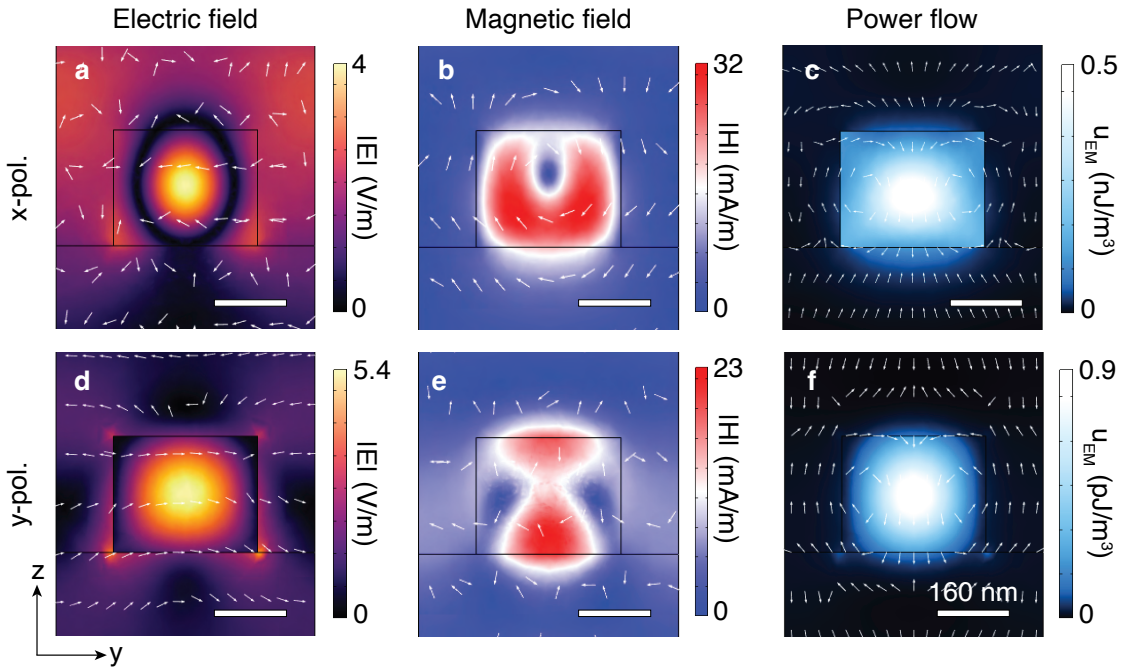

Figure S5: **Electromagnetic behavior of the metasurface in the yz-plane**. (a),(d) The electric field strength (heat map) and direction (arrows) in the unit cell for x- (a) and y-polarization (d). (b),(e) Same as (a),(d) but for the magnetic field. (c),(f) The time-averaged electromagnetic energy density (heat map) and Poynting vector (arrows) in the unit cell for x- (c) and y-polarization (f). All of the images are given in the yz-plane of the metasurface and at the operating wavelength.

The results are given in Fig. S9 for the case of normally incident, x-polarized plane waves illuminating the resonator at the operating wavelength. The 3D (Fig. S9a) and polar radiation patterns (Fig. S9d) show that majority of the light is concentrated in the forward direction. The electromagnetic field behavior in the xz-plane shows field enhancement within the resonator (Fig. S9b-c). The multipole decomposition of the scattering cross section indicates that this is due to an electric dipole resonance (Fig. S9e).

S2.4 Imaging simulations

Simulations of tunable multi-modal microscopy were performed in MATLAB R2022a by the formulations presented in the 'Tunable multi-modal microscopy - principles' section of the main article and in the section S1.1. The optical transfer function of the metasurface that was calculated in COMSOL Multiphysics 6.1 (Fig. S7) was used to model the optical

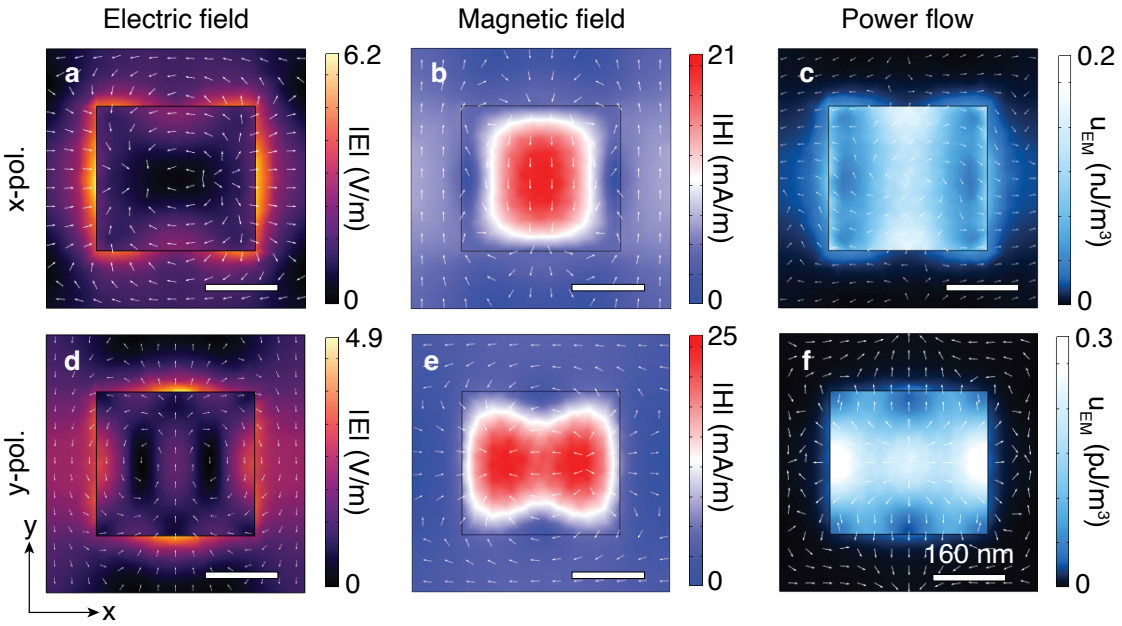

Figure S6: **Electromagnetic behavior of the metasurface in the xy-plane**. (a),(d) The electric field strength (heat map) and direction (arrows) in the unit cell for x- (a) and y-polarization (d). (b),(e) Same as (a),(d) but for the magnetic field. (c),(f) The time-averaged electromagnetic energy density (heat map) and Poynting vector (arrows) in the unit cell for x- (c) and y-polarization (f). All of the images are given in the xy-plane of the metasurface and at the operating wavelength The slice through the z-plane is taken at the interface between the resonator and substrate.

response of the metasurface in Eq. (S6). Three imaging targets were used in the simulations and experiments. The first included an opaque amplitude mask with the word 'Amplitude' and a phase profile of the word 'Phase' (Fig. S10 - top left), which was presented in the main article. The second included the opaque word 'Erythrocyte' and the phase profile of a human red blood cell (Fig. S10 - top middle). Some of the experimental imaging results are presented in Fig. 1a of the main article. The phase profile of the red blood cell was modelled using the empirical optical properties provided in Ref.[9] Lastly, the third imaging target included the opaque word 'T-Lymphocyte' and the phase profile of a leukaemic Jurkat cell (Fig. S10 - top right).[10] The phase profile of the Jurkat cell was modelled using the empirical optical properties from Ref.[11] and the imaging results for both simulation and experiment are presented here.

The simulated imaging results are presented in Fig. S10. The images obtained with x-polarized illumination contained both of the transparent and opaque features of the input

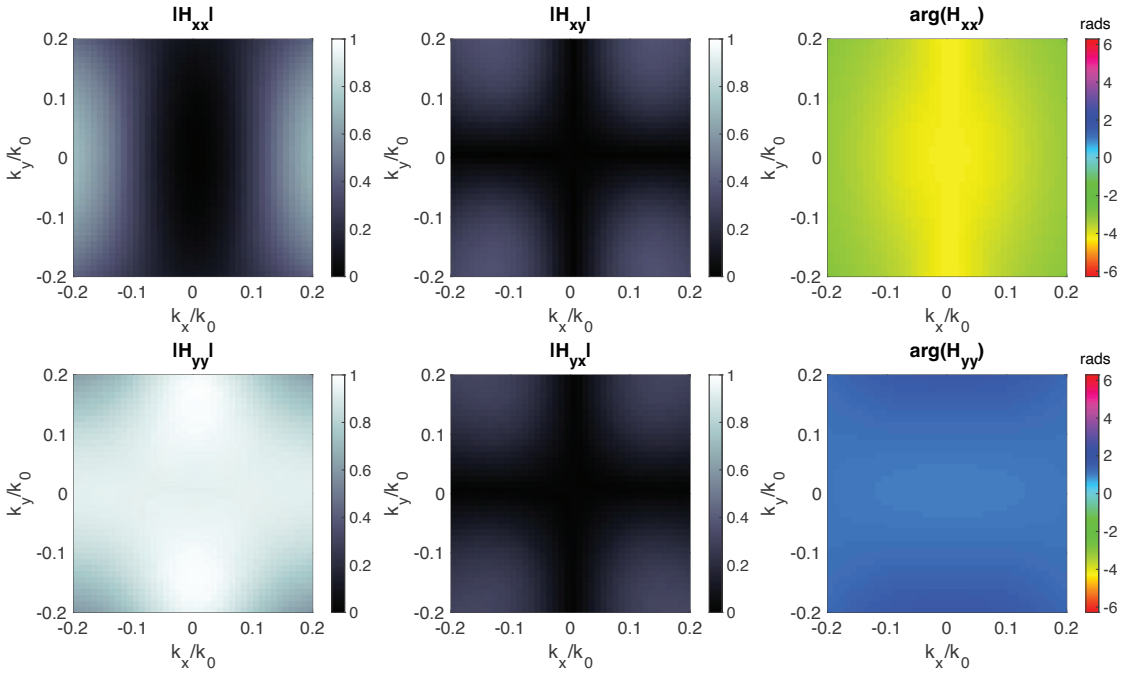

Figure S7: **2D optical transfer function of the metasurface**. The magnitude (first two columns) and phase (last column) of the optical transfer function tensor components at the operating wavelength.

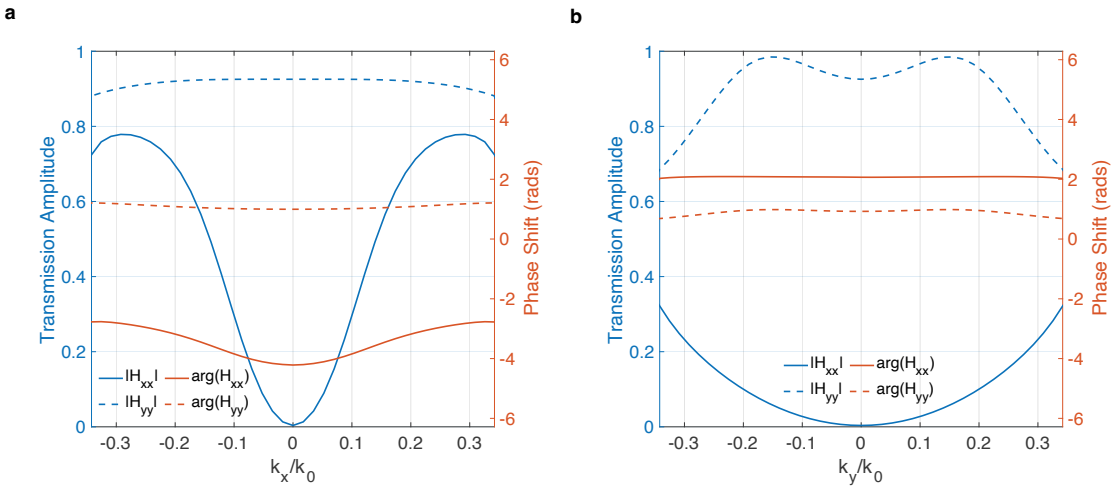

Figure S8: **1D optical transfer function of the metasurface**. (a) The magnitude and phase of the co-polarized components of the optical transfer function along $k_y = 0$. (b) Same as a but along $k_x = 0$.

imaging target (Fig. S10 - middle row). Each of the phase profiles have pseudo-3D contrast visible in the images. On the other hand, only the opaque words are visible in the images obtained with y-polarized illumination (Fig. S10 - bottom row).

Table S1: **Simulated performance metrics of the metasurface.** The performance metrics were obtained through simulations in COMSOL Multiphysics 6.1 at the operating wavelength of 969 nm, corresponding to the electric dipole resonance of the metasurface. Here, $\vec{E}_0$ denotes the electric field of the normally-incident, x-polarized illumination. The values $k_x^{\max}$ and $k_x^{\min}$ denote the spatial frequencies at the edges of the contrast zone. E_t and E_r denote the electric field transmitted through, and reflected from, the metasurface, respectively. P_{cross} and P_{in} denote the cross-polarized and input power, respectively. Lastly, $\Delta\lambda$ is the full width at half-maximum of the transmission minimum at the operating wavelength.

Quantity	Label	Formula	Value
Transmittance	T	$\lvert E_t/E_0\rvert^2$	0.001
Reflectance	R	$\lvert E_r/E_0\rvert^2$	0.993
Absorptance	A	$1-T-R$	≤ 0.006
Quality factor	Q	$\lambda/\Delta\lambda$	17.3
Field enhancement	ΔE	$\max(\lvert E/E_0\rvert)$	6.1
Numerical aperture	NA	$(k_x^{\max}-k_x^{\min})/k_0$	≤ 0.17
Angular response	Θ	$\Delta\lambda/\lambda$	0.06
Polarization conversion efficiency	ϵ_{pol}	$100\%P_{\text{cross}}/P_{\text{in}}$	0.001%
Processing efficiency	η	$\lvert H_{xx}(k_x^{\max},0)\rvert$	79%
Switching contrast (amplitude)	δ	$H_{yy}(0,0)-H_{xx}(0,0)$	93%
Switching contrast (transmittance)	Δ	T_y-T_x	86%

S3 Optical configurations

S3.1 Polarization

The metasurface operates under the excitation by linearly polarized illumination. As in the main article, we define two coordinate systems. The first is the global coordinate system with respect to the optical bench in the experiment. The second is with respect to the metasurface defined by the long axis of the silicon blocks, the short axis and the normal to the metasurface. Assume that the illumination propagates along the global z-axis (optical axis). The metasurface was placed in the global xy-plane with its long axis aligned with the global x-axis. It was then tilted by 2° about the global y- (short) axis. Therefore, with this configuration, x-polarized illumination leads to the production of phase contrast images, while y-polarized illumination leads to bright field images. A schematic of the polarization is given in Fig. S11.

In the imaging experiments, the global x-axis was along the vertical direction and the

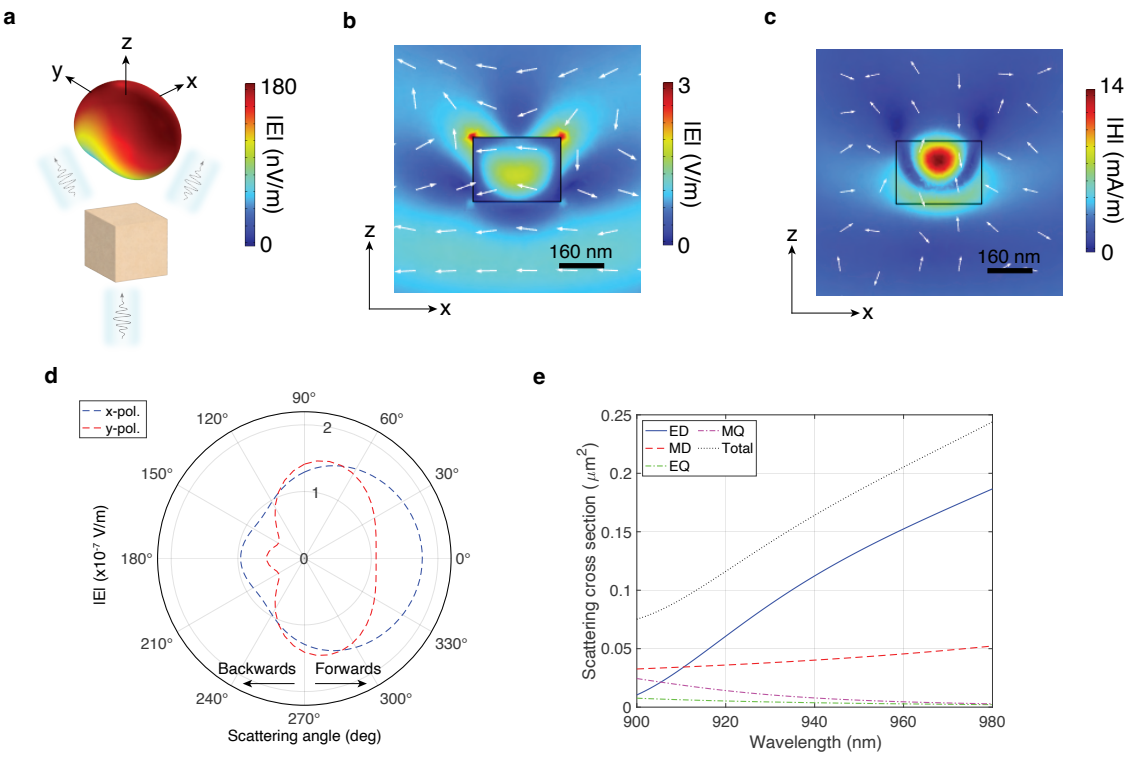

Figure S9: **Optical response of an isolated silicon resonator in air**. (a) The 3D radiation pattern. (b) The electric field strength (heat map) and direction (arrows) when on-resonance in the xz-plane. (c) Same as b but for the magnetic field. (d) The polar radiation plot in the xz-plane for x- and y-polarization. (e) A multipole decomposition of the scattering cross section as a function of the wavelength. The results in (a)-(c) and (e) were obtained with x-polarized illumination at the operating wavelength.

global y-axis was along the horizontal direction. The metasurface was oriented with its long axis along the vertical direction (at normal incidence), as depicted in Fig. S11. To change the polar angle of incidence θ, the metasurface was tilted about the horizontal direction. The illumination was x-polarized when the input polarizer was along the vertical direction. On the other hand, the illumination was y-polarized when the input polarizer was horizontal. The effects of de-polarization and/or cross-polarization by the spatial light modulator (SLM), imaging samples, metasurface and optical components were measured to be negligible. For example, the slight deviations on the polarization set by the polarizer due to diffraction from the SLM was a weak effect.

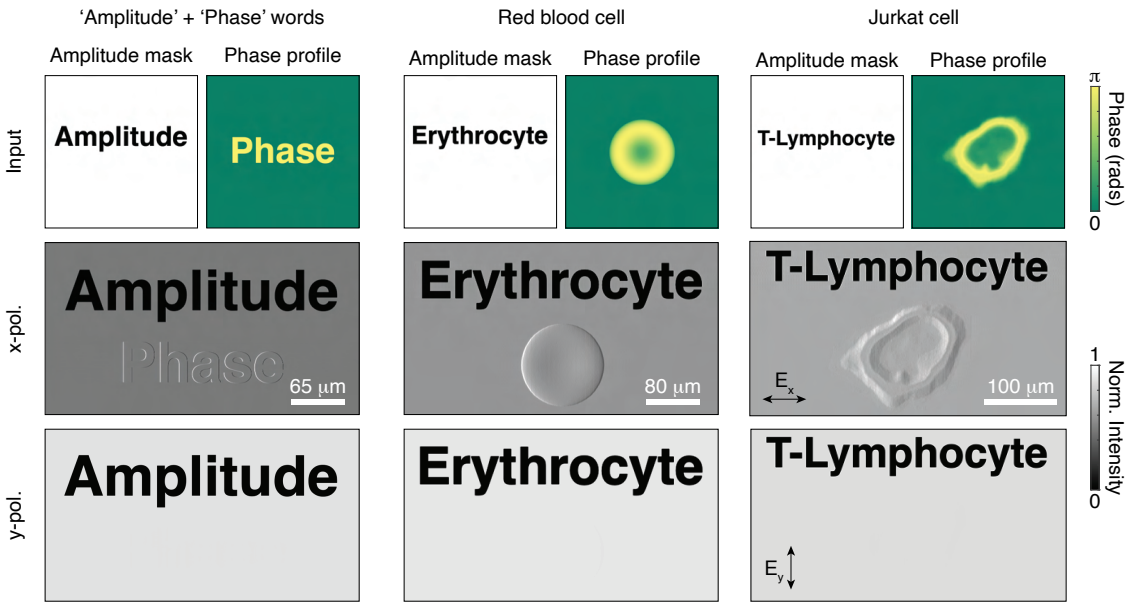

Figure S10: **Simulated tunable multi-modal microscopy with the metasurface**. (First row) The amplitude and phase masks of the input imaging target. (Second row) The output images obtained with x-polarized illumination. (Final row) The output images obtained with y-polarized illumination.

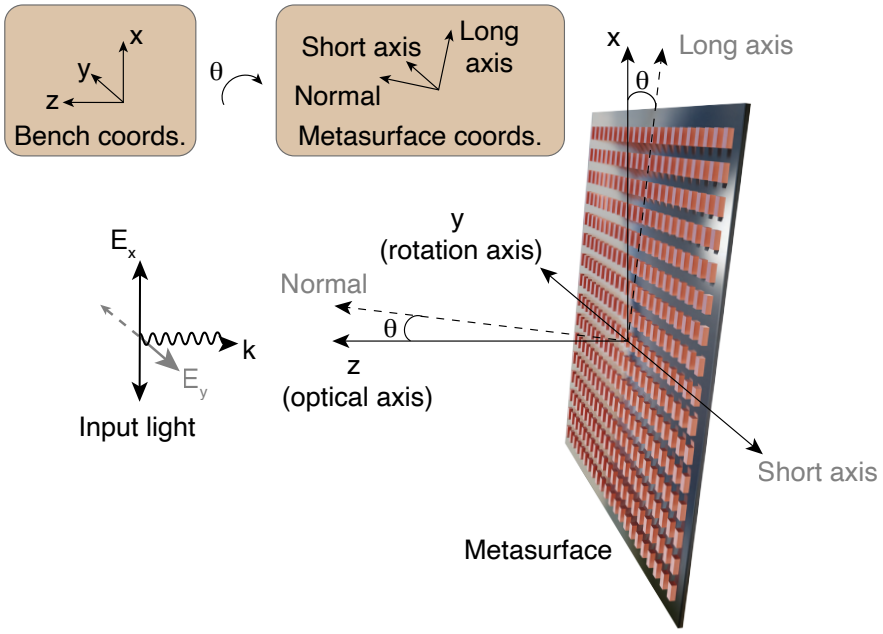

Figure S11: **Polarization**. Schematic of how the polarization is defined and referred to in this article.

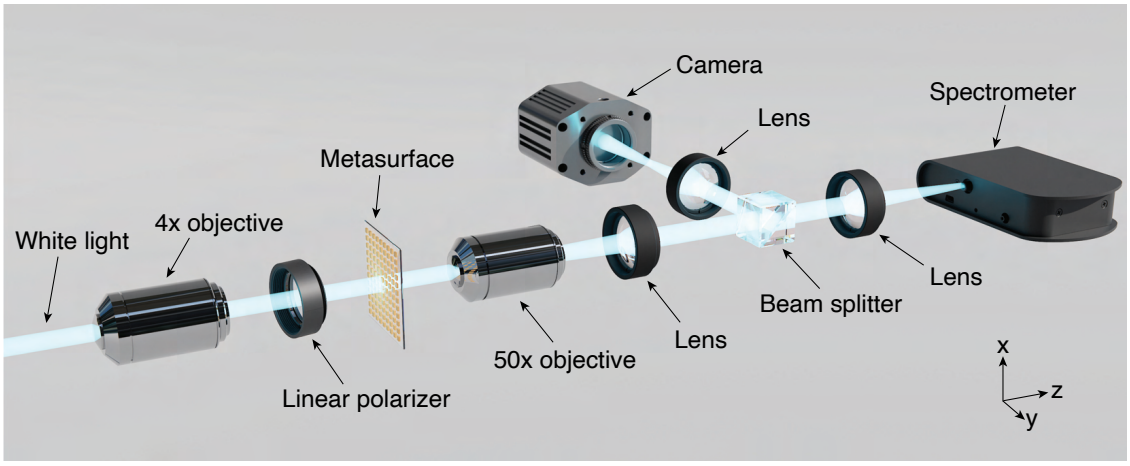

Figure S12: **Normal-incidence spectroscopy configuration**. White light from a halogen lamp was collimated by a microscope objective and linearly polarized. The light transmitted by the metasurface was collected by a second microscope objective and a lens. A second lens focused the transmitted light onto a spectrometer. A beam-splitter was used to simultaneously relay an image of the metasurface onto a camera by a lens.

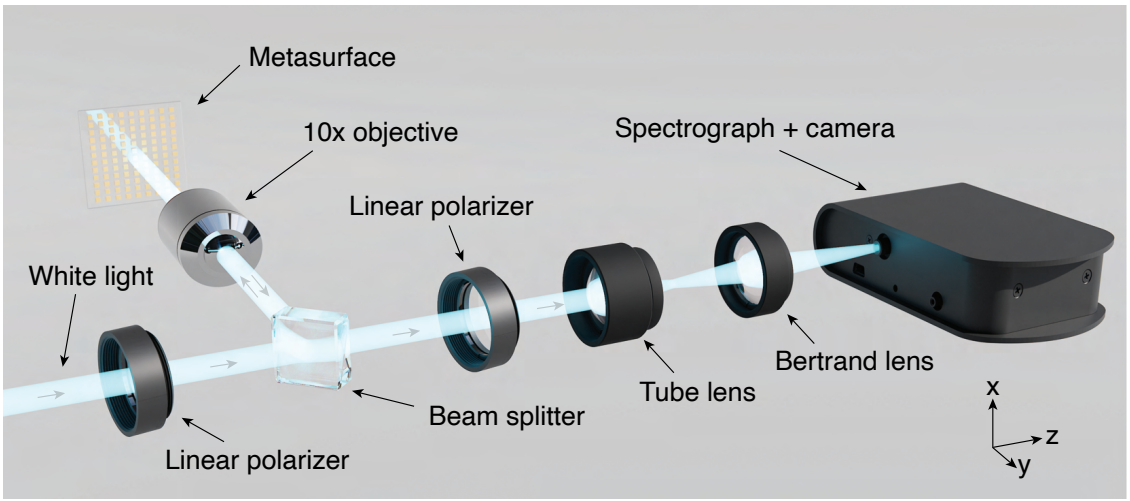

Figure S13: **Angle-dependent spectroscopy via back focal plane imaging**. White light from a halogen lamp was linearly polarized and illuminated the metasurface through a microscope objective. The reflected light from the objective back focal plane was imaged onto a spectrograph/CCD couple with a tube lens and Bertrand lens pair. An analyzer was used before the spectrograph to select specific components of the optical transfer function tensor.

S3.2 Spectrometry

The normal-incidence and angle-dependent spectroscopy experiments are detailed in the Methods section of the main article. Here, schematics of their experimental configurations are shown in Figs. S12 and S13.

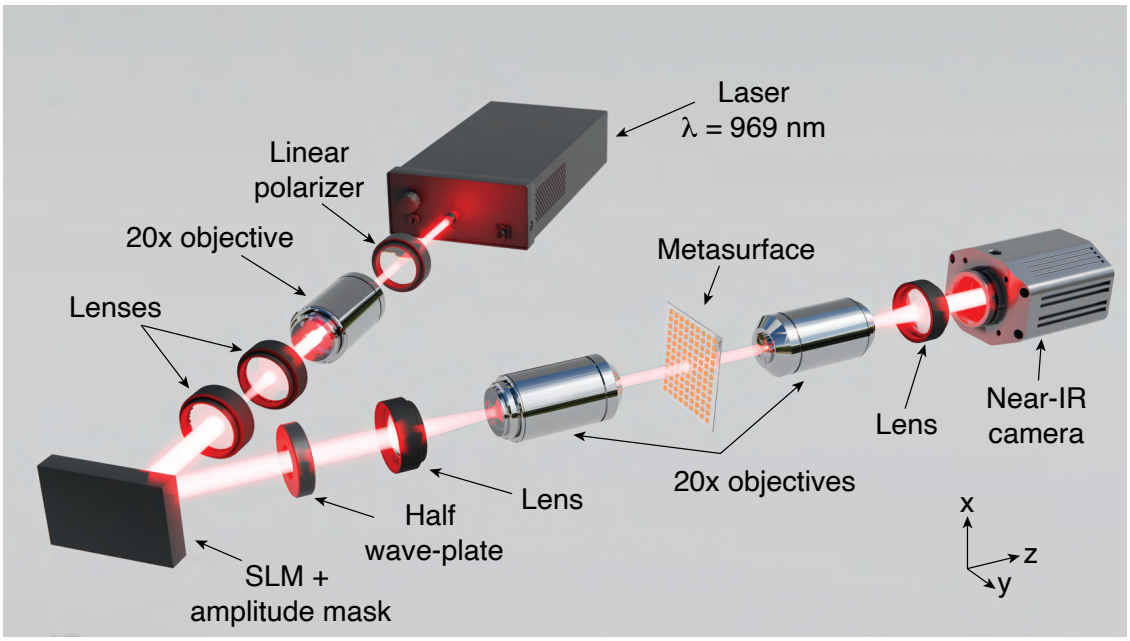

Figure S14: **Experimental configuration for imaging involving a spatial light modulator**. The light from a super-continuum source was linearly polarized and collimated by a microscope objective and two lenses. The lenses expanded the beam to fill the aperture window of the SLM. An amplitude mask was placed in front of the SLM. The light reflected by the SLM was focused into a microscope objective by a lens. The microscope objective produced a small collimated beam containing a de-magnified image of the SLM aperture. The metasurface was placed in the image plane. A half wave-plate was placed before the lens to change the polarization. A microscope objective and lens relayed a magnified image onto a camera.

S3.3 Imaging with a spatial light modulator

The experimental imaging results involving the SLM presented were obtained with the configuration illustrated in Fig. S14. This schematic is also shown in Fig. 3 of the main article.

S3.4 Biological microscopy

The experimental biological imaging results with the metasurface presented in the main article were obtained with the configuration illustrated in Fig. S14. This schematic is also shown in Fig. 4 of the main article.

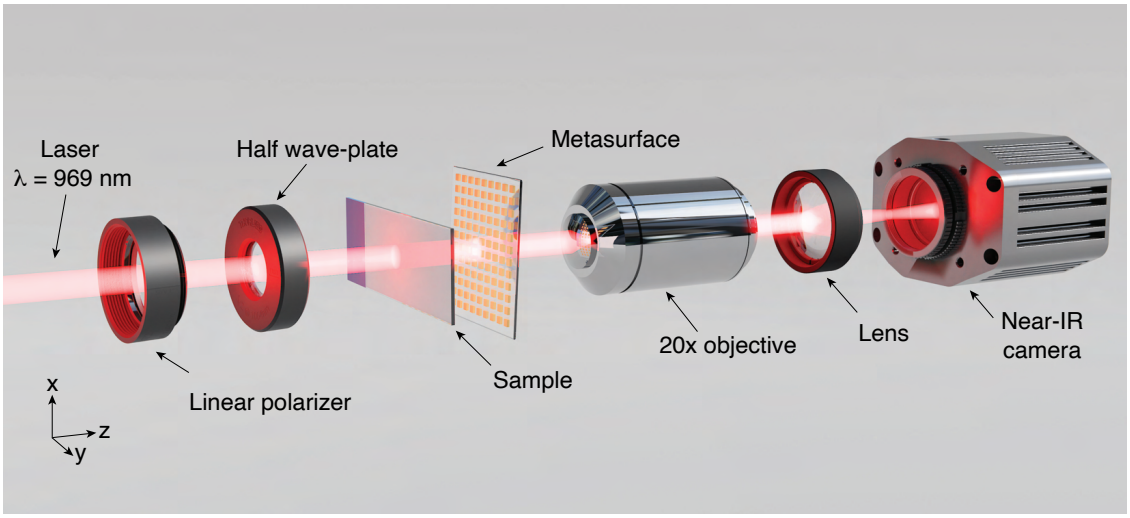

Figure S15: **Bio-imaging configuration**. The light from a super-continuum source was linearly polarized and a half wave-plate was used to control the polarization. The light illuminated a sample and the metasurface was placed after the sample. A microscope objective and lens relayed a magnified image onto a camera.

S4 Additional experimental data

S4.1 Metasurface fabrication

A flowchart of the fabrication process and pictures of the metasurface are given in Fig. S16. The metasurface was fabricated on a 10 mm-thick glass substrate that was 15 mm by 15 mm in size. A thin 23 nm layer of indium tin oxide (ITO) was coated onto the glass substrate to be used as a conducting protector for the electron beam lithography process. Similarly, a thin 10 nm layer of aluminium oxide (Al_2O_3) was coated onto the silicon to be used as a hard protective mask for the etching process.

S4.2 Optical characterization

The angle-dependent spectroscopy experiments were performed with the back focal plane imaging configuration depicted in Fig. S13 and detailed in the Methods section of the main article. The metasurface was oriented such that the angular range would be along the plane of incidence defined by the long axis of the metasurface. The results (Fig. S17)

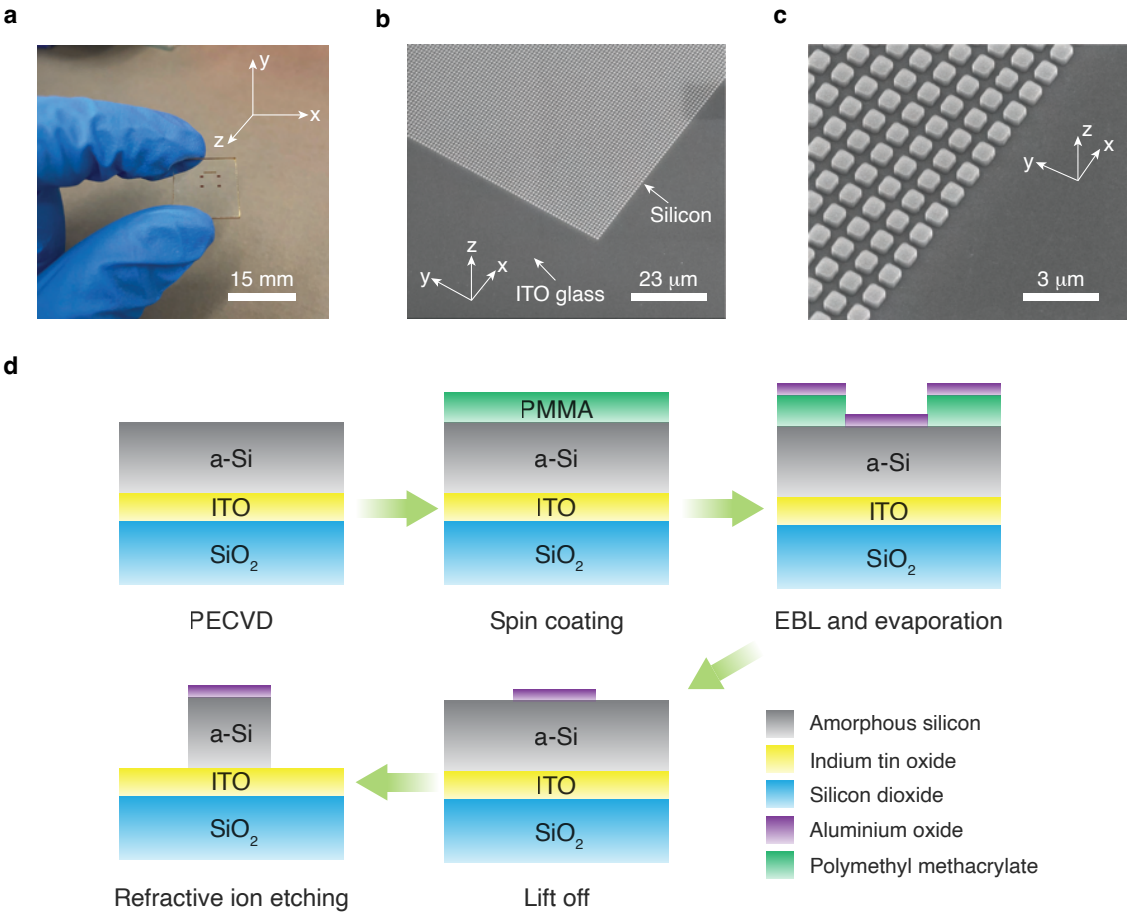

Figure S16: **Fabrication of the metasurface**. (a) A photo of the metasurface fabricated onto a coverslip. (b),(c) Scanning electron microscope images of the metasurface. (d) A flowchart of the fabrication process. Plasma-enhanced chemical vapor deposition is abbreviated to PECVD.

show the reflectance counts as a function of the wavelength and angle for input x- and y-polarized illumination. The former shows strong reflection at normal incidence at the operating wavelength, which decreases in strength as the angle increases. Meanwhile, the latter has a relatively low reflection. Plots of the line profiles along the line segments in Fig. S17 are given in Fig. 2b-ii of the main article in the form of transmission amplitude data.

S4.3 Performance metrics

The experimental performance of the metasurface was quantified through the metrics presented in Table S2. These included the transmittance, reflectance, quality factor, numerical aperture, angular response, processing efficiency and the switching contrast. The results are

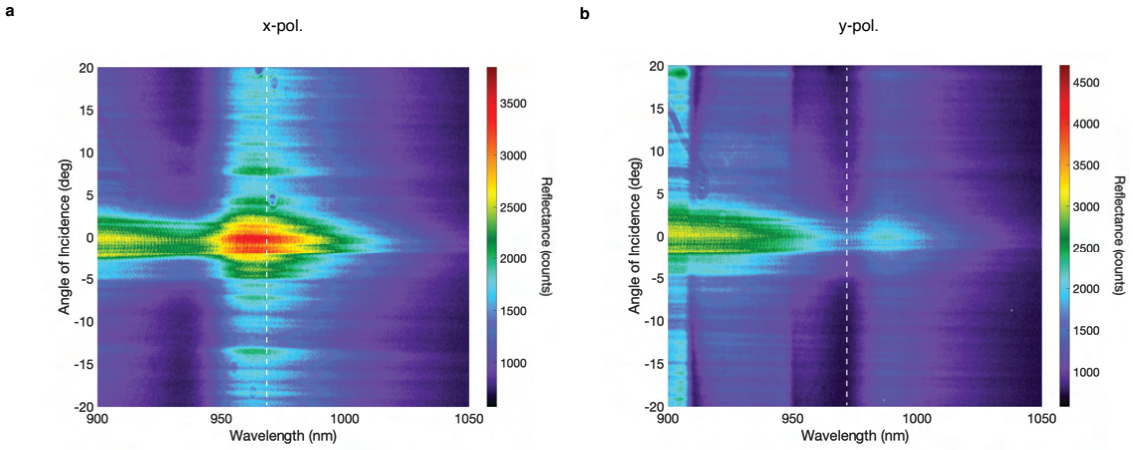

Figure S17: **Angle-dependent spectroscopy via back focal plane imaging**. (a) 2D heat map of the reflectance counts from the metasurface as a function of the wavelength and angle of incidence for px-polarization. (b) Same as a but for y-polarization. The white dashed lines indicate the operating wavelength.

Table S2: **Experimental performance metrics of the metasurface.** The experimental performance metrics obtained at the operating wavelength of 969 nm.

Quantity	Label	Formula	Value
Transmittance	T	$\lvert E_t/E_0\rvert^2$	≥ 0.096
Reflectance	R	$\lvert E_r/E_0\rvert^2$	≤ 0.931
Quality factor	Q	$\lambda/\Delta\lambda$	19.29
Numerical aperture	NA	$(k_x^{\max} - k_x^{\min})/k_0$	≤ 0.17
Angular response	Θ	$\Delta\lambda/\lambda$	0.05
Processing efficiency	η	$\lvert H_{xx}(k_x^{\max}, 0)\rvert$	78%
Switching contrast (amplitude)	δ	$H_{yy}(0,0) - H_{xx}(0,0)$	60%
Switching contrast (transmittance)	Δ	$T_y - T_x$	71%

tabulated in Table S2 and can be compared to the simulations in Table S1.

S4.4 Imaging experiments

The multi-modal microscopy experiments involving the SLM were performed with the three different imaging targets set out in section S2.4. The imaging results with the 'Amplitude' and 'Phase' words in the imaging target were presented in Fig. 3 of the main article. The imaging results of the red blood cell are given in Fig. S18 and the results of the Jurkat cell are given in Fig. S19.

The red blood cell (Fig. S18b) and Jurkat cell (Fig. S19b) were visualized in the images

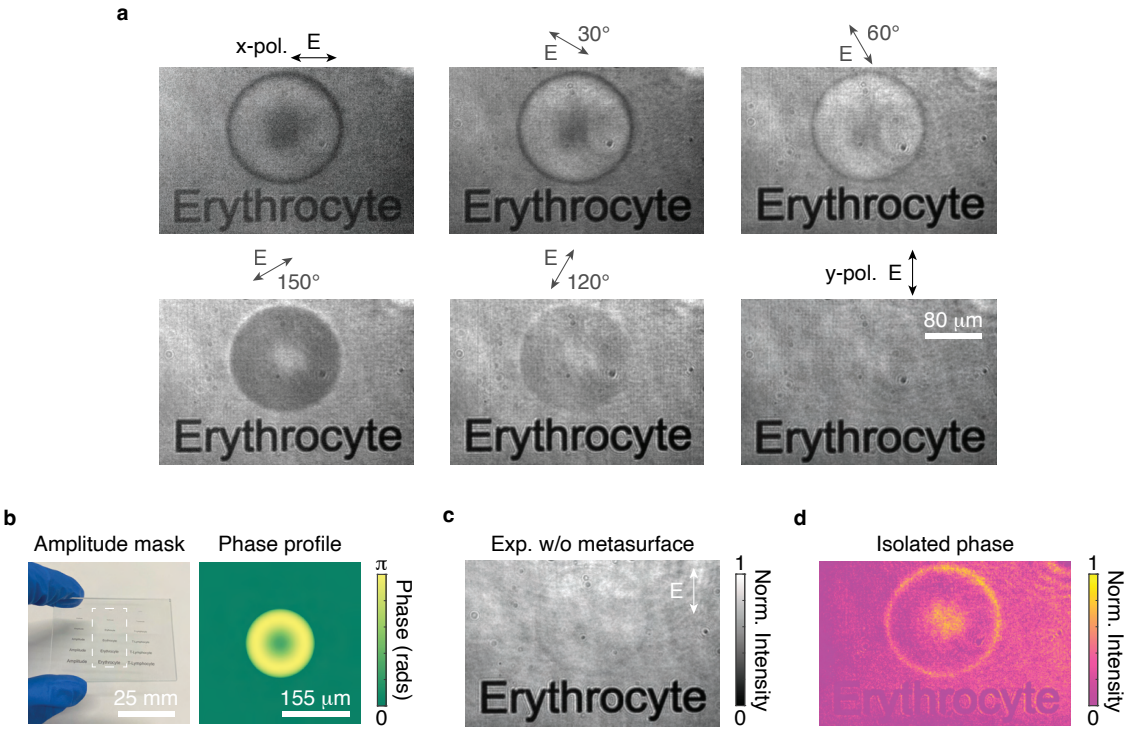

Figure S18: **Tunable multi-modal microscopy experiments of samples produced by a spatial light modulator - red blood cell**. (a) The experimental images obtained with the metasurface for different polarization states of the illumination at the operating wavelength. (b) The input imaging target included an amplitude mask and a phase profile on the spatial light modulator. (c) The experimental image obtained in the absence of the metasurface. (d) The image obtained by subtracting the image obtained with x-polarized illumination from the image obtained with y-polarized illumination.

obtained under x-polarized illumination (Figs. S18a and S19a). The contrast of these features had a pseudo-3D appearance. On the other hand, the words 'Erythrocyte' (Fig. S18b) and 'T-Lymphocyte' (Fig. S19b) were visible in all of the images obtained in the experiment (Figs. S18a and S19a), independent of the polarization. In particular, only these features were visible in the images obtained under y-polarization. These images were similar to the images taken in the absence of the metasurface (Figs. S18c and S19c). The images were combined to qualitatively isolate the phase contrast by subtracting the images obtained with x-polarization from those obtained with y-polarization (Figs. S18d and S19d).

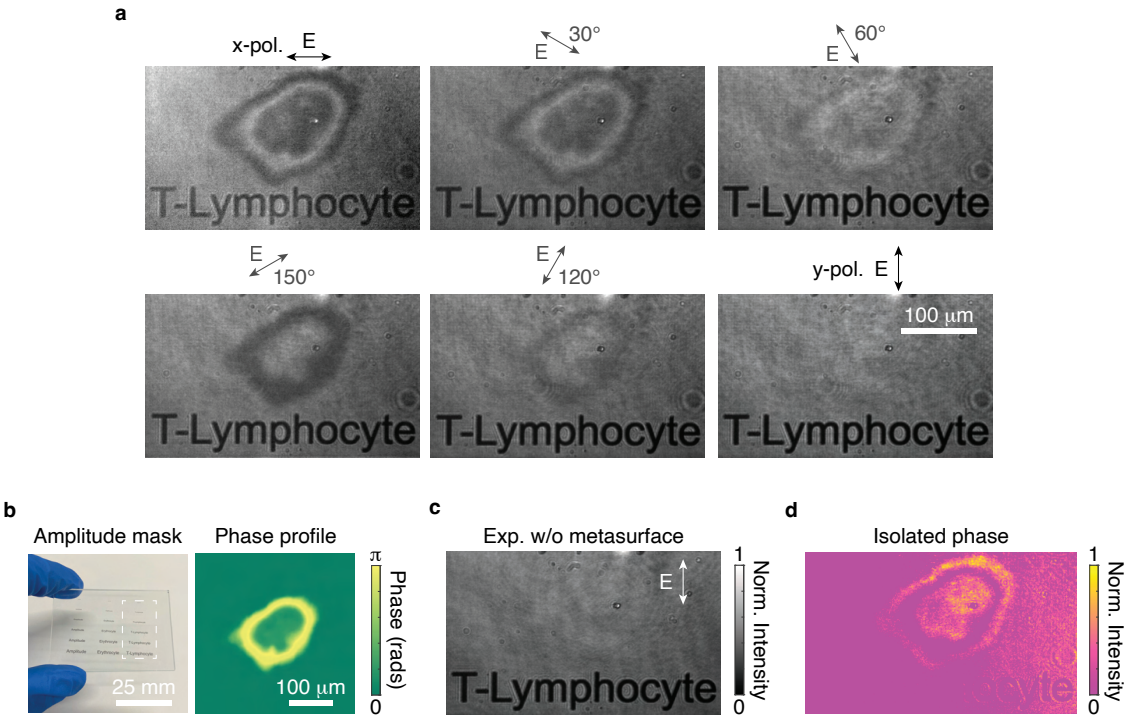

Figure S19: **Tunable multi-modal microscopy experiments of samples produced by a spatial light modulator - Jurkat cell**. (a) The experimental images obtained with the metasurface for different polarization states of the illumination at the operating wavelength. (b) The input imaging target included an amplitude mask and a phase profile on the spatial light modulator. (c) The experimental image obtained in the absence of the metasurface. (d) The image obtained by subtracting the image obtained with x-polarized illumination from the image obtained with y-polarized illumination.

S4.5 Biological imaging

As discussed in the main article, the thickness of the breast tissue sample was a challenge for the imaging modalities used in the experiments. The metasurface and the DIC microscope were capable of highlighting the architectural structure within the tissue, even at the higher thickness provided by the microtomy blade sectioning of the whole tissue blocks. This capacity can allow for the identification of normal architectural patterns within the tissue and those which are abnormal, e.g. tumours often form aberrant architectural structural arrangements. However, identifying more complex structures or lower order cellular detail is uncertain, as the imaged area included only a small number of structures in a simple and benign arrangement.

Instead, a more ideal application would be the preparation of cellular material rather than formalin-fixed, paraffin embedded in-situ tissue that requires a thicker tissue sample. In this case, the imaging samples would be generated by smearing fresh tissue to directly transfer individual and clusters of cells onto a glass slide, rather than an entire section of tissue. This produces a thinner sample with cells juxtaposed on a background slide, rather than remaining embedded in their native tissue environment. These thinner samples would provide a greater differential between individual and groups of cells and the background glass slide. Furthermore, it may facilitate a better generation of cellular level imaging data.

S4.6 Experimental videos

Four experimental videos are included as supporting material. The first (Video S1) is a recording of an experiment made on the polarization switching ability of the metasurface. By using the experimental configuration detailed in the 'Multi-modal microscopy - biological samples and polarization switching' sub-section of the Methods section of the main article, an image of the metasurface was captured by a camera under normally incident illumination at the operating wavelength. The video shows how the performance of the metasurface changes as a function of the polarization.

The second video (Video S2) is a recording of an imaging experiment with the metasurface. By using the experimental configuration detailed in the 'Multi-modal microscopy - spatial light modulator' sub-section of the Methods section of the main article, contrast related to the phase profile of a Jurkat cell was visualized by the metasurface. The phase profile disappears as the polarization of the illumination was changed.

The third (Video S3) and fourth (Video S4) videos are recordings of some of the experimental tests made for imaging *C. elegans* with the metasurface. The videos show how the nematodes appear with and without the metasurface, as well as a live nematode moving in the sample. The latter demonstrates the capacity for the metasurface to be used for dynamic monitoring of samples.

References

(1) Wesemann, L.; Davis, T. J.; Roberts, A. Meta-optical and Thin Film Devices for All-optical Information Processing. *Applied Physics Reviews* **2021**, *8*, 031309.

(2) Goodman, J. W. *Introduction to Fourier Optics*; McGraw-Hill, 1996.

(3) Terekhov, P. D.; Babicheva, V. E.; Baryshnikova, K. V.; Shalin, A. S.; Karabchevsky, A.; Evlyukhin, A. B. Multipole analysis of dielectric metasurfaces composed of nonspherical nanoparticles and lattice invisibility effect. *Physical Review B* **2019**, *99*, 045424.

(4) Mie, G. Beiträge zur Optik trüber Medien, speziell kolloidaler Metallösungen. *Annalen der Physik* **1908**, *330*, 377.

(5) Bohren, C. F.; Huffman, D. R. *Absorption and Scattering of Light by Small Particles*; John Wiley & Sons, 1983.

(6) Mühlig, S.; Menzel, C.; Rockstuhl, C.; Lederer, F. Multipole Analysis of Meta-atoms. *Metamaterials* **2011**, *5*, 64–73.

(7) Fruhnert, M.; Fernandez-Corbaton, I.; Yannopapas, V.; Rockstuhl, C. Computing the T-matrix of a Scattering Object with Multiple Plane Wave Illuminations. *Beilstein Journal of Nanotechnology* **2017**, *8*, 614–626.

(8) Shi, Z.; Zhu, A. Y.; Li, Z.; Huang, Y.-W.; Chen, W. T.; Qiu, C.-W.; Capasso, F. Continuous angle-tunable birefringence with freeform metasurfaces for arbitrary polarization conversion. *Science Advances* **2020**, *6*, eaba3367.

(9) Evans, E.; Fung, Y.-C. Improved measurements of the erythrocyte geometry. *Microvascular Research* **1972**, *4*, 335–347.

(10) Schneider, U.; Schwenk, H.-U.; Bornkamm, G. Characterization of EBV-genome negative "null" and "T" cell lines derived from children with acute lymphoblastic leukemia and leukemic transformed non-Hodgkin lymphoma. *International Journal of Cancer* **1977**, *19*, 621–626.

(11) Zhang, Q.; Zhong, L.; Tang, P.; Yuan, Y.; Liu, S.; Tian, J.; Lu, X. Quantitative refractive index distribution of single cell by combining phase-shifting interferometry and AFM imaging. *Scientific Reports* **2017**, *7*, 2532.